ACS OMEGA

Open Access

This article is licensed under CC-BY-NC-ND 4.0

http://pubs.acs.org/journal/acsodf

Article

New Design Method of a Supersonic Steam Injection Nozzle and Its Numerical Simulation Verification

Qianhui Wang, Zhanxi Pang,* Cong Tian, and Jiajie Chen

Cite This: *ACS Omega* 2023, 8, 44485−44496

Read Online

ACCESS | Metrics & More | Article Recommendations

ABSTRACT: Steam huff-*n*-puff in horizontal wells often had limitations, such as uneven steam injection and low reservoir utilization. To improve steam injection efficiency, a new method for designing a supersonic nozzle was proposed based on the principles of aerodynamics and thermodynamics. The nozzle featured a tapering section, a throat, and a diverging section. The best geometric shape of the tapering section was the Witoszynski curve. A set of nozzle size designs were established, and the size parameters were optimized. The results showed that the nozzle could inject steam into the formation at supersonic speed and it had the characteristics of constant flow rate and uniform development of the steam chamber. According to the steam Reynolds number and the good aggregation distribution characteristics of the size design model, three sequential nozzles of 3.0, 5.0, and 6.5 mm were formed based on the throat. When the throat diameter was 5.0 mm, the tapering length was 4.3 mm, the diverging length was 5.5 mm, the throat length was 3.0 mm, the inlet diameter was 9.8 mm, and the outlet diameter was 6.2 mm. Numerical simulations indicated that the pressure drop loss during steam huff-*n*-puff injection in horizontal wells was within 10%. It was of great significance to establish the nozzle size design model of the steam injection effect of horizontal wells.

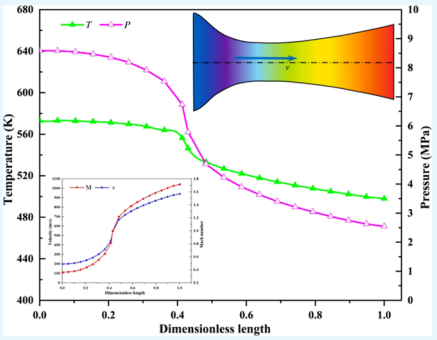

1. INTRODUCTION

With the global decline in conventional oil reserves, there has been a growing recognition of the significance of heavy oil as an important unconventional oil and gas resource. China possessed abundant reserves of heavy oil, with proven and controlled reserves of 16×10^8 t, positioning it as the fourth-largest producer of heavy oil worldwide, following the United States, Canada, and Venezuela.[1−5] At that time, the development of heavy oil reservoirs heavily relied on thermal recovery techniques, including steam huff-*n*-puff, steam flooding, and steam-assisted gravity drainage (SAGD).[6−8] In the production process of heavy oil through horizontal wells, whether using the SAGD technique with dual horizontal wells or the horizontal well steam huff-*n*-puff technique, a challenge arose in achieving uniform steam injection. Nonuniform steam injection led to poor reservoir utilization, which significantly hampered the overall development efficiency.[9−12]

In response to those challenges, Chinese heavy oil fields such as Liaohe, Shengli, and Xinjiang initially adopted automatic steam allocation technology. Although this approach partially alleviated the issue of uneven steam injection, its complex process hindered widespread application.[13−15] Subsequently, technologies such as segmented perforation completion, variable density perforation completion, and central tubing completion were developed. However, these techniques had limited control over steam injection or reservoir steam absorption profiles, making it difficult to ensure sufficient uniformity in the steam absorption profile.[16−19] Later on, a commonly employed approach involved the utilization of steam flow control methods, relying on specially designed steam control valves to achieve uniform steam injection.[20−22] In 2014, Liu[23] developed adjustable steam control valves and the corresponding retrieval tools to address the issue of non-adjustability of steam valves in horizontal wells. This innovation led to the establishment of a more refined process for achieving a uniform steam injection in horizontal wells. After large-scale implementation in the Liaohe oilfield, the average exploitation rate in the horizontal section increased by 21%, leading to substantial improvement in the oil recovery performance.

In addition to the aforementioned approaches for enhancing steam injection uniformity, increasing attention has been devoted to innovative wellbore configurations. Cutting-edge steam injection column structures, such as single-pipe, dual-pipe, multipoint injection, and segregated injection in dual horizontal wells, have gained widespread adoption both domestically and globally, showcasing favorable field perform-

Received: March 18, 2023
Revised: October 17, 2023
Accepted: November 3, 2023
Published: November 15, 2023

© 2023 The Authors. Published by American Chemical Society

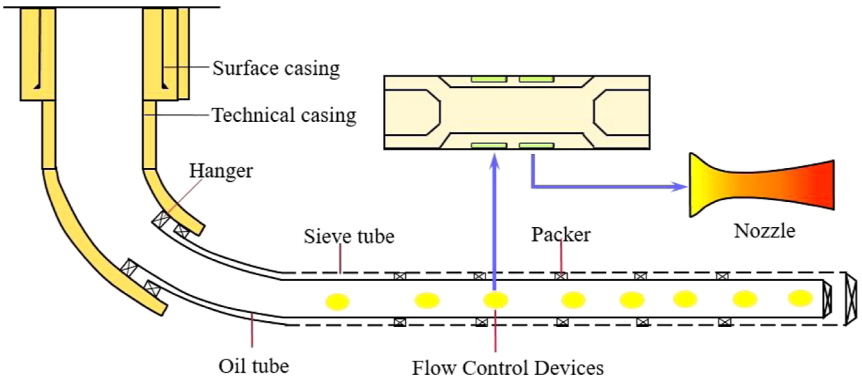

Figure 1. Horizontal wellbore structure for heavy oil.

ance.[24] Dual-pipe injection, which capitalized on the dual-point injection feature of the main and auxiliary pipes, had the added advantage of facilitating simultaneous steam injection at the heel and toe of the horizontal section. This method effectively mitigated the heel-toe effect in horizontal wells and promoted a more uniform steam injection profile.[25] In 2019, Dong et al.[26] proposed integration of flow control devices (FCDs) with dual-pipe injection technology for steam injection in horizontal wells. Experimental results revealed that this approach boosted heavy oil production by approximately 35%, indicating that dual-tubing injection technology could significantly improve the recovery of heavy oil reservoirs. However, single-pipe and dual-pipe injection methods had yet to fully resolve the issues of uneven steam absorption in the reservoir and poor displacement efficiency, and the then-existing design of tubing structures had yet to achieve optimal application.

The FCD technology was widely employed in oil fields worldwide for the extraction of heavy oil resources.[27] Research on FCDs has primarily focused on throttling control,[28−30] with the nozzle playing a crucial role in this regard. Therefore, the design of the nozzle was vital for ensuring steam injection uniformity. As shown in Figure 1, it depicts the schematic diagram of a horizontal wellbore structure for heavy oil. FCD usage improved steam conformance and prevented unwanted steam breakthroughs, improving thermal efficiency in the steam injection process.[31−34] FCDs were commonly classified into outflow control devices (OCDs), inflow control devices, and bidirectional devices. OCDs were specifically designed for horizontal steam injection wells, facilitating the regulation of steam flow within the horizontal section and the formation of steam chambers. At that time, the installation of OCDs in the steam injection column of horizontal wells had emerged as a promising technology for addressing the issue of nonuniform steam injection.[35] However, only a limited number of oil companies, such as Weatherford, Halliburton, and Conoco-Phillips, have devoted resources to the research and experimentation of OCDs. Although nozzle-type OCD devices were employed in the field, there was a lack of relevant foundations for optimizing the design of nozzle structures.[36] Considering the widespread application of horizontal well steam injection technology in the exploitation of heavy oil reservoirs and the notable advantages exhibited by OCDs in enhancing steam injection uniformity, conducting research on the structural design and optimization of nozzles to improve steam injection uniformity in horizontal wells carried substantial significance.[37,38]

2. NEW DESIGN METHOD OF A SUPERSONIC STEAM INJECTION NOZZLE

2.1. Basic Assumptions of the Nozzle Design. To simplify the analysis of steam flow characteristics, certain assumptions were commonly applied when considering the use of steam flow through critical injection nozzles. These assumptions were based on the fundamental principles of thermodynamics.[39] The following assumptions were made:

(1) The steam flow within the nozzle was characterized by high velocity, short residence time, and negligible heat exchange with the surrounding environment. As a result, the steam flow could be treated as an adiabatic process.[40]
(2) Apart from the nozzle inlet, the steam flowing through the nozzle could be described by the ideal gas equation of state. This assumption allowed for simplified calculations and analysis of the steam flow behavior.
(3) Steam flow could be treated as an isentropic process, neglecting the influence of nonisentropic factors such as shock waves.[41]
(4) The steam flow was assumed to be one-dimensional and in a steady-state condition. This assumption simplified the analysis by disregarding variations in flow parameters along different dimensions.

Based on the aforementioned fundamental assumption, in the design of the nozzle structure, it was assumed that the flow of steam within the nozzle constituted an isentropic adiabatic process.

2.2. State Equation of Steam in the Nozzle. The steam state equation flowing in the supersonic nozzle is shown as follows.

The pressure equation is shown as eq 1.

$$\frac{p_m}{p_n} = \left(\frac{\rho_m}{\rho_n}\right)^k = \left(\frac{T_m}{T_n}\right)^{k/k-1} = \left(\frac{1+\frac{k-1}{2}M_m^2}{1+\frac{k-1}{2}M_n^2}\right)^{-k/k-1} \quad (1)$$

The density equation is shown as eq 2.

$$\frac{\rho_m}{\rho_n} = \left(\frac{1+\frac{k-1}{2}M_m^2}{1+\frac{k-1}{2}M_n^2}\right)^{-1/k-1} \quad (2)$$

Temperature equation is shown as eq 3.

$$\frac{T_m}{T_n} = \left(\frac{1+\frac{k-1}{2}M_m^2}{1+\frac{k-1}{2}M_n^2}\right)^{-1} \quad (3)$$

https://doi.org/10.1021/acsomega.3c01835
ACS Omega 2023, 8, 44485−44496

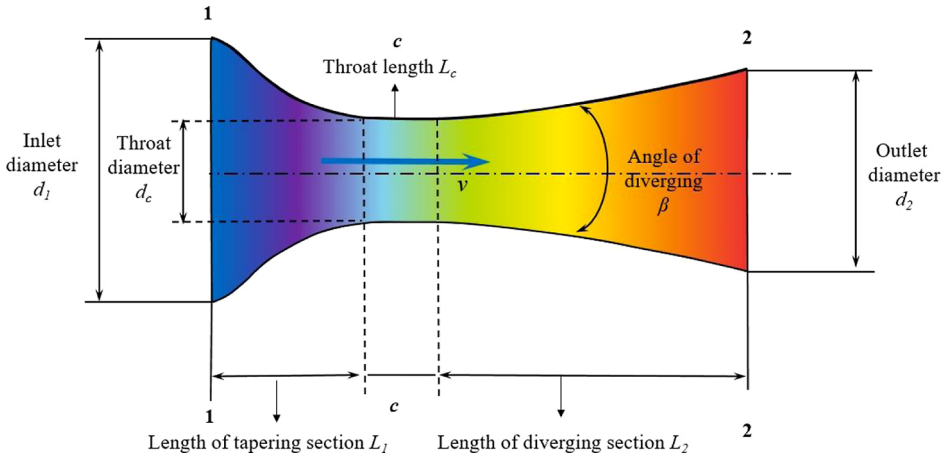

Figure 2. Schematic diagram of the supersonic steam injection nozzle structure.

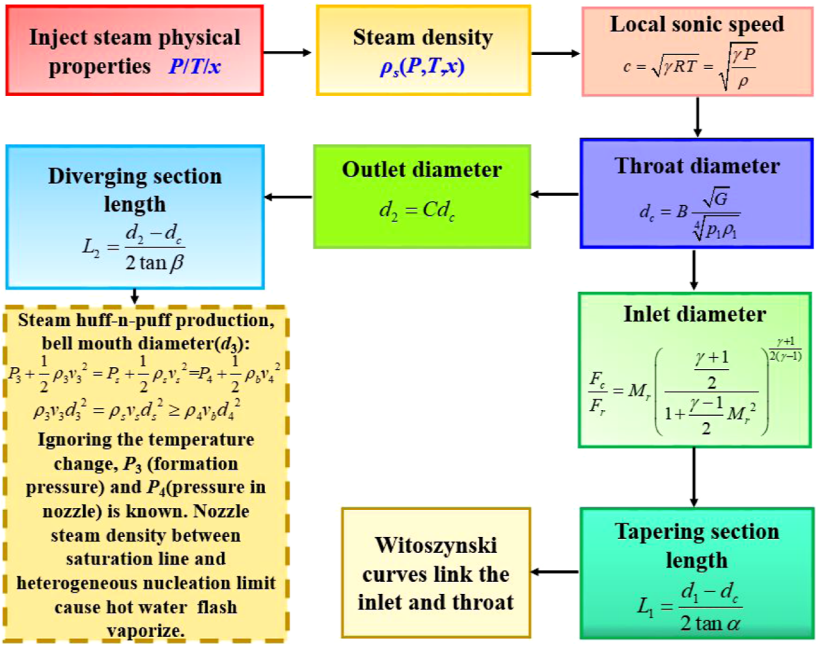

Figure 3. Diagram of the nozzle design.

where p_m and p_n are the steam pressure on any two sections in the nozzle, Pa; ρ_m and ρ_n are the density of the steam on any two sections in the nozzle, kg/m^3; and T_m and T_n are the temperatures of the steam in any two sections of the nozzle, K.

2.3. Basic Structure of the Supersonic Nozzle. The aerodynamic formula satisfied by the supersonic nozzle is shown in eq 4.

$$\frac{dF}{F} = (M^2 - 1)\frac{dv}{v} \tag{4}$$

where F is any cross-sectional area within the nozzle, m^2; v is the flow velocity of the steam in the nozzle, m/s; and M is the Mach number, dimensionless.

Based on the Mach number, the nozzle was commonly classified into three types: tapering type, diverging type, and a combination of tapering and diverging types (supersonic type). From the working principle of the supersonic steam injection nozzle, which aimed to decrease pressure and increase steam velocity, it was evident that during the steam flow within the nozzle $dp < 0$ and $du > 0$.

For the tapering nozzles, $dF < 0$ and $M < 1$ can be obtained. Considering the practical application in oil fields, when utilizing steam huff-*n*-puff technology in horizontal wells for heavy oil extraction, the steam injection velocity often remained subsonic, below the speed of sound. In light of this, the tapering nozzle could serve as the initial section of the supersonic steam injection nozzle. For the diverging nozzle, $dF > 0$ and $M > 1$ can be obtained. This showed that the velocity of steam in the diverging nozzle could be increased to supersonic speed, allowing for the steam to flow out of the formation at supersonic speed. As a result, the diverging nozzle was suitable for the end section of the supersonic injection nozzle. When $M = 1$, the velocity of steam reached sonic speed at the throat.

The initial section (tapering type) and the final section (diverging type) were connected by a parallel straight-throat section, forming the fundamental structure of the supersonic injection nozzle, as shown in Figure 2.

2.4. Theoretical Design Method of the Supersonic Nozzle. The design methodology for a supersonic critical steam injection nozzle was as follows: First, the density of the steam

https://doi.org/10.1021/acsomega.3c01835
ACS Omega 2023, 8, 44485−44496

was calculated based on its properties such as pressure (P), temperature (T), and dryness fraction (x). Subsequently, the local sonic speed (c) was determined by using the calculated steam density. The throat diameter was then obtained by considering the sonic flow rate and steam properties. Solving for the throat diameter not only provided the nozzle outlet diameter and the length of the diverging section but also allowed for the determination of the tapering section length by solving for the inlet diameter. Ultimately, the inlet and throat were connected using a Witoszynski profile. During steam huff-*n*-puff, after obtaining the length of the diverging section, the bell mouth diameter was calculated using the Venturi principle to facilitate flash evaporation of the hot water. The detailed design process is illustrated in Figure 3.

3. STRUCTURE OPTIMIZATION DESIGN OF THE SUPERSONIC NOZZLE

3.1. Throat Section Design. *3.1.1. Nozzle Throat Diameter Design.* Steam entered the nozzle at subsonic speeds, and its velocity reached the local sonic speed at the throat, known as the supersonic velocity (v_{cr}). At this point, the steam state parameters at the throat reached a critical state, denoted as critical parameter (cr), including the pressure, density, temperature, and flow rate at the throat represented as p_{cr}, ρ_{cr}, and T_{cr}, respectively. Referring to Figure 2, the steam inlet section was labeled as 1−1, the outlet section as 2−2, and the throat section as c−c. The parameters at the nozzle inlet were p_1, ρ_1, and T_1, while at the outlet, they were p_2, ρ_2, and T_2. Equation 5 was derived from eq 1.

$$\frac{p_{cr}}{p_1} = \left(\frac{\rho_{cr}}{\rho_1}\right)^k = \left(\frac{T_{cr}}{T_1}\right)^{k/k-1} = \left(\frac{1+\frac{k-1}{2}M_{cr}^2}{1+\frac{k-1}{2}M_1^2}\right)^{-k/k-1} \tag{5}$$

Assuming that the maximum mass flow rate through the nozzle throat was G_{max}, eq 6 was obtained from the continuity equation.

$$G_{max} = F_c v_{cr} \rho_{cr} \tag{6}$$

Due to $v_{cr} \gg v_1$, $M_{cr} = 1$, the simultaneous eqs 5 and 6 were derived.

$$F_c = \frac{G_{max}}{v_{cr}\rho_{cr}} = \frac{1}{\sqrt{k\left(\frac{2}{k+1}\right)^{k+1/k-1}}} \times \frac{G_{max}}{\sqrt{p_1\rho_1}} \tag{7}$$

where F_c is the critical cross-sectional area of the throat, m^2; G_{max} is the mass flow of the nozzle steam, kg/s; P_1 is the absolute pressure at the nozzle inlet, Pa; and ρ_1 is the steam density at the nozzle inlet, kg/m^3.

The section in the nozzle could be regarded as a circle. According to the relationship between the area and diameter of the circle, G was used instead of G_{max}, and eq 7 was rewritten as eq 8.

$$d_c = B\frac{\sqrt{G}}{\sqrt[4]{p_1\rho_1}} \tag{8}$$

where d_c is the throat diameter, mm; B is the throat diameter calculation coefficient, $B = \frac{1}{\sqrt{0.9\pi\sqrt{k\left(\frac{2}{k+1}\right)^{k+1/k-1}}}}$; and G is the mass flow rate of steam in the nozzle, kg/h.

3.1.2. Nozzle Throat Length Design. The supersonic steam injection nozzle was composed of three parts, and its throat geometry was usually designed as a slender parallel straight section. It has been proved by engineering practice that the design of the nozzle throat as a slender horizontal straight section can not only stabilize the airflow but also overcome the defect that the throat is vulnerable to damage without a straight pipe section, causing the diameter to change.[42] Therefore, the optimal geometry shape of the nozzle throat is a horizontal straight section. According to the actual application requirements, the throat length L_c was generally 3−4 mm.

3.2. Diverging Design. *3.2.1. Nozzle Cross-Sectional Area Ratio Design.* In the study, it was assumed that the flow of steam within the nozzle followed an isentropic adiabatic process. The local speed of sound is shown in eq 9.

$$c = \sqrt{kp/\rho} = \sqrt{kRT} \tag{9}$$

where c is the local speed of sound, m/s; and R is the gas constant.

The cross-sectional area ratio of the nozzle was a key parameter to design the nozzle size. Combine pressure eqs 1 and 9 to obtain the area ratio of any two sections in the nozzle as shown in eq 10.

$$\frac{F_m}{F_n} = \frac{M_n}{M_m}\left(\frac{1+\frac{k-1}{2}M_m^2}{1+\frac{k-1}{2}M_n^2}\right)^{k+1/2(k-1)} \tag{10}$$

Therefore, it was easy to discover from eq 10 that the adiabatic index was a constant value, and the ratio of cross-sectional areas between any two sections within the nozzle was only dependent on the steam Mach numbers.

3.2.2. Nozzle Outlet Diameter Design. According to pressure eq 1, the pressure ratio of the nozzle outlet to inlet could be obtained. As $v_2 \gg v_1$, so $1+\frac{k-1}{2}M_1^2 \approx 1$. Therefore, eq 11 could be obtained.

$$M_2 = \sqrt{\frac{2}{k-1}\left[\left(\frac{p_2}{p_1}\right)^{k-1/k} - 1\right]} \tag{11}$$

The ratio of the nozzle outlet cross-sectional area to the throat cross-sectional area could be obtained according to eq 10, as shown in eq 12.

$$\frac{F_2}{F_c} = \frac{1}{M_2}\left(\frac{1+\frac{k-1}{2}M_2^2}{1+\frac{k-1}{2}}\right)^{k+1/2(k-1)} \tag{12}$$

The pressure ratio between the inlet and outlet of the nozzle was set to E, as shown in eq 13.

$$E = p_1/p_2 \tag{13}$$

where E is the expansion ratio, dimensionless.

According to the relationship between the circle area and the diameter, combined with the above equation, the nozzle outlet diameter is shown in eq 14.

$$d_2 = Cd_c \tag{14}$$

where C is the calculation coefficient of the nozzle outlet diameter, dimensionless,

https://doi.org/10.1021/acsomega.3c01835
ACS Omega 2023, 8, 44485−44496

$C = \left[\frac{k-1}{2}\left(\frac{2}{k+1}\right)^{k+1/k-1}\right]^{1/4}\left(\frac{E^{k+1/k}}{E^{k-1/k}}\right)^{1/4}$; and d_2 is the outlet diameter, mm.

For saturated steam, the value of k was 1.135. Given the nozzle throat diameter, the nozzle outlet diameter could be obtained, as shown in eq 15.

$$d_2 = 0.3937\left(\frac{E^{1.8811}}{E^{1.8811}-1}\right)^{1/4}\cdot d_c = 0.2937\left(\frac{E^{1.8811}}{E^{1.8811}-1}\right)^{1/4}\cdot\frac{\sqrt{G}}{\sqrt[4]{p_1\rho_1}} \quad (15)$$

According to eq 15, it was evident that the nozzle outlet diameter depended on the pressure ratio between the nozzle inlet and outlet as well as the steam conditions at the nozzle inlet. This highlighted the need to consider the specific steam conditions at the nozzle inlet when designing the nozzle outlet diameter.

3.2.3. Length Design Diverging Section.

$$L_2 = \frac{d_2 - d_c}{2\tan\beta} \quad (16)$$

where β is the divergent angle, °.

The diverging section is often designed with a circular and straight line, Foelsch[43] analytical method and straight line, and tapered tube structure. The primary purpose of the diverging section was to accelerate the steam, which initially had a velocity equal to the speed of sound, to supersonic speeds, facilitating its flow out of the nozzle and into the formation. Combined with literature research and engineering practice, it was recommended to use divergent angles ranging from 14 to 19°.[44,45] A divergence angle that was too small would result in a longer expansion distance, leading to increased friction and pressure losses. Conversely, an excessively large divergence angle would cause inadequate steam expansion, thereby impacting the steam acceleration along the diverging section.

3.3. Tapering Section Design. *3.3.1. Design of the Nozzle Inlet Diameter.* After consulting relevant literature, Chen et al.[46] proposed a design for supersonic nozzles that recommended the nozzle inlet be made as large as possible within structural constraints and that it should be at least larger than the nozzle outlet diameter. Therefore, the inlet diameter of the nozzle was designed based on the calculated nozzle outlet diameter.

3.3.2. Tapering Section Length Design.

$$L_1 = (d_1 - d_c)/2\cdot\tan\alpha \quad (17)$$

where α is the tapering angle, °.

According to eq 17, the length of the tapering section was inversely proportional to the tapering angle. A smaller tapering angle resulted in a longer tapering section. Through an analysis of the influence of the tapering angle on the steam flow field, it was concluded that a tapering angle too small would cause significant friction losses, while a tapering angle too large would result in uneven steam flow. Therefore, the taper angle should neither be too large nor too small.[47,48] In order to ensure stable acceleration of steam during the flow process in the tapering section, the typical range for the tapering angle was between 30 and 60°.

3.3.3. Geometry Optimization of the Tapering Section. The geometric shape of the taper section was not unique. Different geometric shapes resulted in diverse flow fields within the nozzle, thereby affecting the energy of the steam ejected from the nozzle. Based on a literature review, it was evident that many researchers paid little attention to the geometric shape of the tapering section during the design process, often assuming that the optimal shape was the Witoszynski curve.[49] In this study, with a fixed length of the tapering section, the starting point and end point of the section were assumed as points A and B, respectively, and a comparison was made among the parabola, Witoszynski curve, and straight line passing through these two points. Figure 4 illustrates the schematic of these three curves.

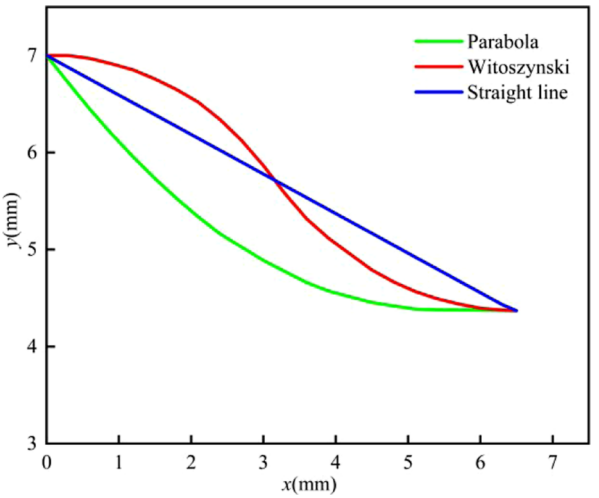

Figure 4. Schematic diagram of different curves.

Based on MATLAB simulation results, the length of the flow path for each curve and the time required for the mass point to move along the curve were obtained, as shown in Figure 5. The

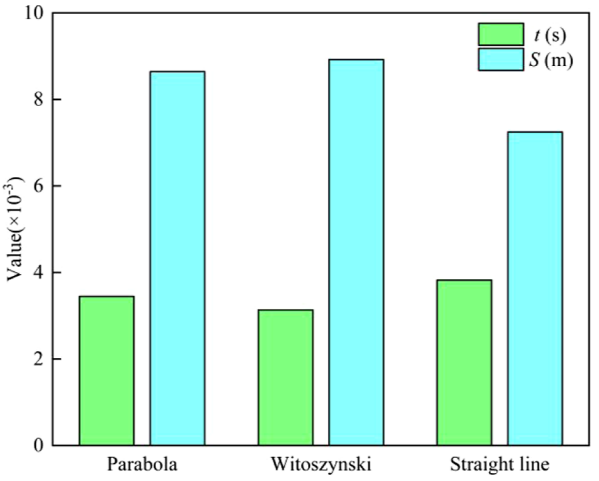

Figure 5. Comparison result diagram.

comparative results demonstrated that the Witoszynski curve had the longest flow passage length but the shortest travel time, followed by the parabola, while the straight flow passage length was the shortest but the mass point took the longest time. This finding confirmed the superiority of the Witoszynski curve as the optimal choice. Therefore, designing the geometry of the tapering section as a Witoszynski curve was more appropriate.

https://doi.org/10.1021/acsomega.3c01835
ACS Omega 2023, 8, 44485−44496

Table 1. Structural Parameters of the Supersonic Steam Injection Nozzle under Different Steam Injection Conditions

flow (t/h)	pressure (MPa)	tapering section length L_1 (mm)	diverging section length L_2 (mm)	throat length L_c (mm)	inlet diameter d_1 (mm)	throat diameter d_c (mm)	outlet diameter d_2 (mm)
1.0	15.0	2.2	2.9	3.0	5.4	2.6	3.2
1.0	10.0	2.5	3.2	3.0	5.7	2.9	3.6
1.0	5.0	2.9	3.8	3.0	6.2	3.4	4.2
3.0	15.0	3.8	5.0	3.0	9.4	4.5	5.6
3.0	10.0	4.3	5.5	3.0	9.8	5.0	6.2
5.0	15.0	5.0	6.4	3.0	12.1	5.8	7.2
5.0	10.0	5.5	7.1	3.0	12.7	6.4	8.0
3.0	5.0	5.1	6.5	3.0	10.7	5.9	7.3
5.0	5.0	6.5	8.5	3.0	13.9	7.6	9.5

Table 2. Calculation Results of Reynolds Number of Steam

flow (t/h)	steam dryness	dry steam density (kg/m^3)	saturated water density (kg/m^3)	wet steam density (kg/m^3)	dry steam viscosity (mPa·s)	saturated water viscosity (mPa·s)	wet steam viscosity (mPa·s)	Reynolds number
1.00	0.40	92.76	610.13	403.18	0.02	0.08	0.06	177.38
1.00	0.40	54.59	691.09	436.49	0.02	0.09	0.06	163.25
1.00	0.40	4.38	775.86	467.26	0.02	0.10	0.07	143.69
3.00	0.40	92.76	610.13	403.18	0.02	0.08	0.06	532.14
3.00	0.40	54.59	691.09	436.49	0.02	0.09	0.06	489.75
5.00	0.40	4.38	775.86	467.26	0.02	0.10	0.07	718.43
5.00	0.40	92.76	610.13	403.18	0.02	0.08	0.06	886.90
3.00	0.40	54.59	691.09	436.49	0.02	0.09	0.06	489.75
5.00	0.40	4.38	775.86	467.26	0.02	0.10	0.07	718.43

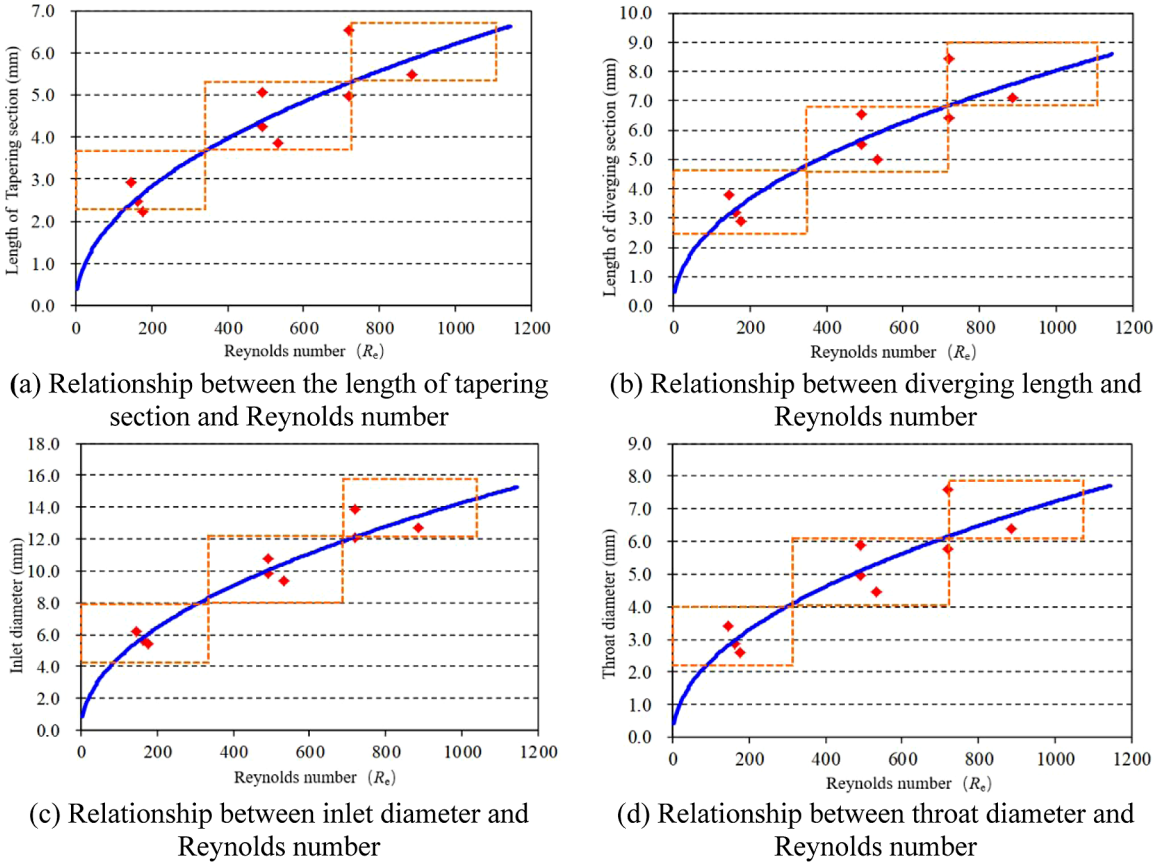

(a) Relationship between the length of tapering section and Reynolds number

(b) Relationship between diverging length and Reynolds number

(c) Relationship between inlet diameter and Reynolds number

(d) Relationship between throat diameter and Reynolds number

Figure 6. Relationship between the axial and radial dimensions of the nozzle shaft and Reynolds number.

https://doi.org/10.1021/acsomega.3c01835
ACS Omega 2023, 8, 44485−44496

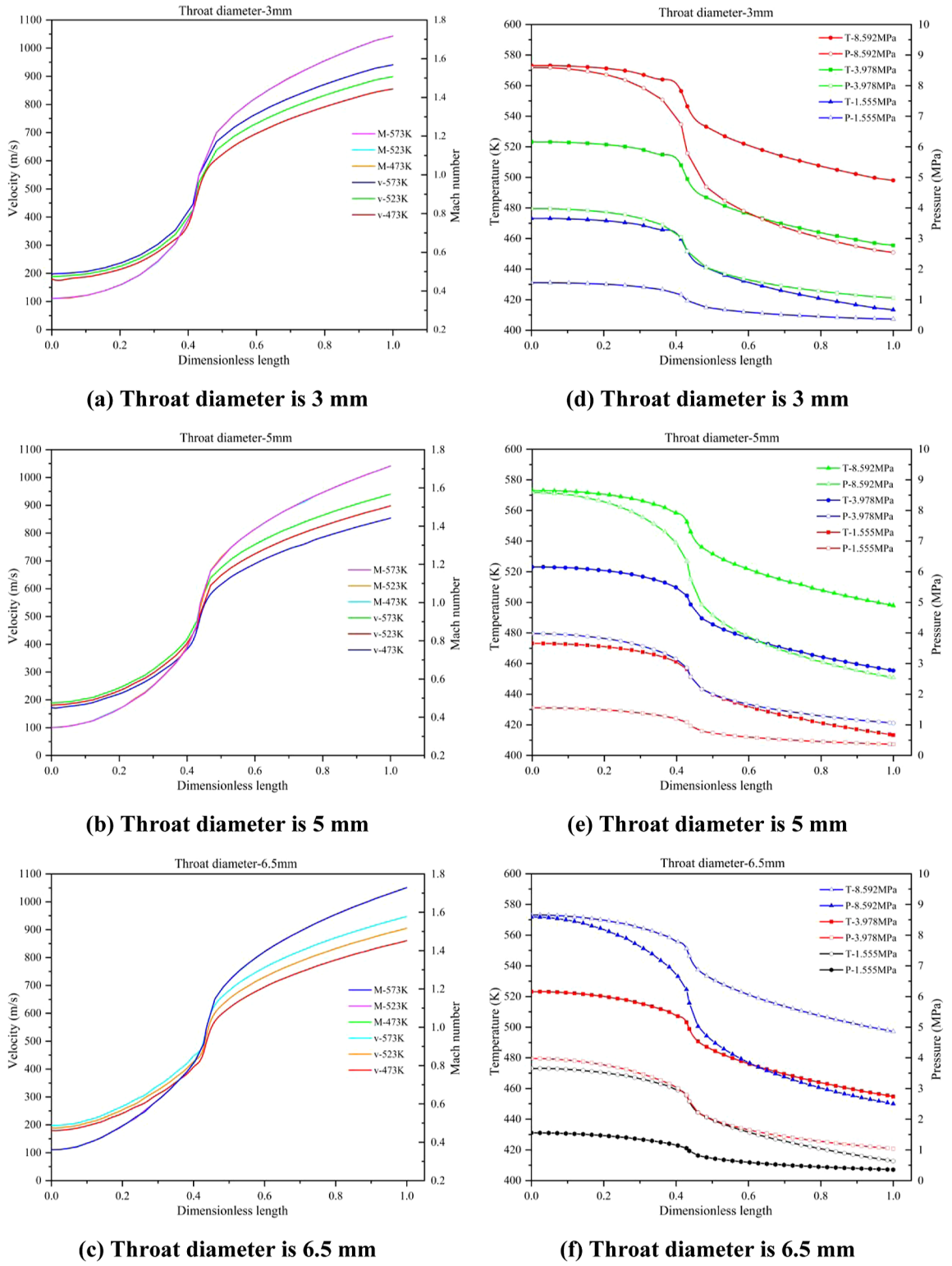

Figure 7. Analysis of steam flow characteristics under different nozzle throat diameters.

4. STRUCTURE DETERMINATION OF THE SUPERSONIC NOZZLE

4.1. Optimization Design of the Nozzle Structure. In the context of steam injection in horizontal wells, we selected injection pressures of 5, 10, and 15 MPa, along with injection rates of 1, 3, and 5 t/h, to calculate the optimal dimensions of the supersonic steam injection nozzle. The specific calculation results are presented in Table 1.

According to the Reynolds number calculation formula[50] (as shown in eq 18), the Reynolds number of steam in the supersonic steam injection nozzle was calculated, and the results are shown in Table 2.

https://doi.org/10.1021/acsomega.3c01835
ACS Omega 2023, 8, 44485−44496

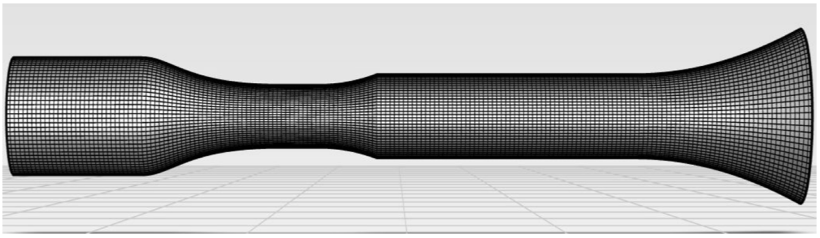

Figure 8. Front view of the supersonic steam injection nozzle with a throat diameter of 3.0 mm.

$$R_e = \frac{\rho v d}{\mu} \tag{18}$$

where R_e is the Reynolds number, dimensionless; d is the nozzle diameter, m; ρ is the fluid density, kg/m^3; v is the flow rate, m/s; and μ is the viscosity, Pa·s.

Based on the analysis of the relationship between the Reynolds number (R_e) of steam within the nozzle and the axial−radial dimensions of the nozzle, it was concluded that the lengths of the tapering and diverging sections, as well as the inlet diameter and throat diameter of the nozzle, exhibited a favorable clustering distribution pattern with respect to the steam Reynolds number, as shown in Figure 6a−d, respectively. Utilizing this favorable clustering distribution pattern, three series of throat diameters were designed: 3, 5, and 6.5 mm, for different steam injection flow rates.

4.2. Analysis and Discussion. Based on the aerodynamic equation and the nozzle size design model, the steam velocity and Mach number were calculated for throat diameters of 3.0, 5.0, and 6.5 mm.

As shown in Figure 7a−c, the variations in velocity and Mach number along the nozzle were calculated using the aerodynamic equation for nozzle inlet temperatures of 473, 523, and 573 K. The results demonstrated that the velocity increased continuously as the steam passed through the supersonic steam injection nozzle, especially with a significant acceleration at the throat section. Moreover, higher steam temperatures resulted in greater outlet velocities. The Mach number trends remained consistent for different temperatures at the same throat diameter.

As shown in Figure 7d−f, the variations in saturation pressure and saturation temperature along the nozzle were calculated using the steam state equation for nozzle inlet pressures of 1.555, 3.978, and 8.592 MPa. The results indicated a gradual decrease in saturation temperature and saturation pressure along the nozzle. Additionally, as the throat diameter increased, the decreasing trends of saturation temperature and saturation pressure in the tapering section became more pronounced. When the flow velocity reached supersonic in the diverging section, the trends of saturation pressure and saturation temperature remained consistent across different throat diameters.

The installation of structurally optimized supersonic steam injection nozzles on the steam injection column in horizontal wells offers the following advantages:

(1) After steam entered the nozzle and passed through the tapering section to reach the throat, the velocity increased from subsonic to local sonic speed. In this process, the flow of steam no longer followed the principle of "higher velocity at smaller cross-sections and lower velocity at larger cross-sections". Instead, as the cross-section increased, the velocity accelerated. When the steam left the throat and entered the diverging section, it was accelerated to supersonic speed, enabling supersonic flow into the reservoir.

(2) The structurally optimized supersonic steam injection nozzle exhibited a constant flow rate feature. The steam reached local sonic speed at the throat and maintained a constant velocity at sonic speed. Even when the external reservoir pressure decreased, the steam velocity at the throat remained unchanged. The magnitude of local sonic speed depended on the steam's state (temperature, pressure, and density). Therefore, by selecting different nozzle throat diameters, different constant flow rates could be achieved.

(3) The supersonic steam injection nozzle reduced pressure losses, enhanced steam injection stability, improved steam dryness, and promoted uniform development of the steam chamber. When the geometrical design of the tapering section followed the Witoszynski curve and the diverging section was a linear straight line, the nozzle underwent gradual changes in diameter without abrupt transitions, resulting in minimal energy losses.

5. VERIFICATION OF NUMERICAL SIMULATION

5.1. Grid Division and Model Building. A three-dimensional model of the supersonic nozzle was created in SolidWorks based on the dimensions mentioned earlier. Mesh generation was carried out using Workbench Meshing. Given that the two-phase gas−liquid flow inside the nozzle involved a high Reynolds number turbulent flow, local mesh refinement near the wall was performed to enhance the accuracy of the simulation results. The model was partitioned into three sets of meshes, consisting of 140,000, 350,000, and 500,000 elements. To ensure the accuracy of the computations, the choice was made to employ 350,000 elements for the numerical simulation.

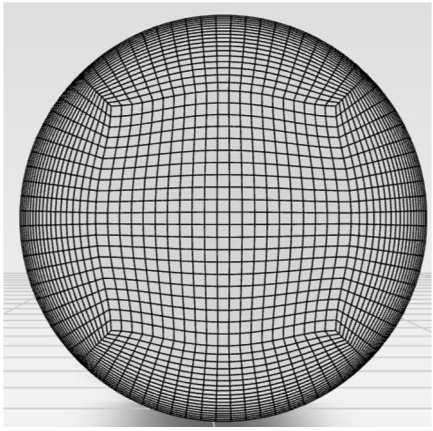

Figure 9. Top view of the supersonic steam injection nozzle with a throat diameter of 3.0 mm.

https://doi.org/10.1021/acsomega.3c01835
ACS Omega 2023, 8, 44485−44496

Table 3. Throat Diameter of 3.0 mm of the Supersonic Nozzle Injection Process Pressure Drop Calculation Results

steam injection speed (t/h)	steam injection temperature (K)	steam injection dryness	inlet gauge pressure (MPa)	outlet gauge pressure (MPa)	pressure drop (MPa)	pressure drop loss (%)
0.1	473	0.5	2.005	1.900	0.105	5.237
4.1	473	0.5	2.636	2.377	0.259	9.825
4.1	523	0.5	2.798	2.541	0.257	9.185
4.1	473	0.7	2.721	2.486	0.235	8.637

Table 4. Throat Diameter of 5.0 mm of the Supersonic Nozzle Injection Process Pressure Drop Calculation Results

steam injection speed (t/h)	steam injection temperature (K)	steam injection dryness	inlet gauge pressure (MPa)	outlet gauge pressure (MPa)	pressure drop (MPa)	pressure drop loss (%)
0.1	473	0.5	1.910	1.900	0.01	0.524
4.1	473	0.5	1.038	0.941	0.097	9.345
4.1	523	0.5	1.078	0.985	0.094	8.627
4.1	473	0.7	1.008	0.932	0.076	7.540

Table 5. Throat Diameter of 6.5 mm of the Supersonic Nozzle Injection Process Pressure Drop Calculation Results

steam injection speed (t/h)	steam injection temperature (K)	steam injection dryness	inlet gauge pressure (MPa)	outlet gauge pressure (MPa)	pressure drop (MPa)	pressure drop loss (%)
4.1	473	0.5	1.555	1.437	0.118	7.588
0.1	473	0.5	2.005	1.900	0.105	5.237
4.1	523	0.5	2.798	2.547	0.251	8.971
4.1	473	0.7	1.572	1.486	0.086	5.471
5.6	473	0.5	1.985	1.807	0.178	8.967

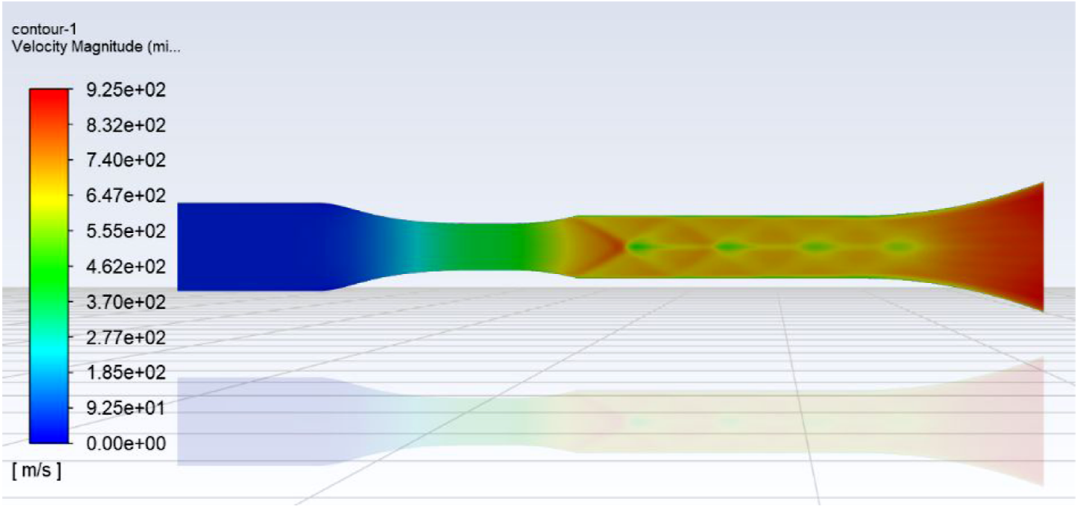

Figure 10. Velocity nephogram with a throat diameter of 3 mm during steam huff-*n*-puff.

As illustrated in Figures 8 and 9, these represent the front and top views of a critical steam injection nozzle with a throat diameter of 3 mm.

5.2. Numerical Simulation Verification. Simulation calculations were performed by using Fluent software. Water vapor was modeled as a compressible ideal gas, and liquid water was treated as an incompressible fluid. A pressure-based steady-state solver was selected. The momentum, turbulent kinetic energy, and turbulent dissipation rate were all solved by using a second-order upwind scheme. The standard k-ε (standard-epsilon) turbulence model was employed, and the walls were assumed to be smooth and no-slip. The inlet boundary condition was set as a mass flow inlet and the outlet as a pressure outlet with an outlet gauge pressure of 1.9 MPa. In cases where the outlet flow became supersonic, the outlet gauge pressure was no longer specified but was calculated internally within the flow field. Setting the outlet gauge pressure was done for ease of iterative computation.

Steam injection velocities were chosen at 0.1, 4.1, and 5.6 t/h, with steam injection temperatures of 200 and 250 °C and steam dryness fractions of 0.5 and 0.7. As shown in Tables 3−5, four sets of steam parameters were selected for numerical simulation research with throat diameters of 3, 5, and 6.5 mm. In the numerical simulations, the inlet and outlet pressures were computed, and the corresponding pressure drop losses were determined. The results indicated that an increase in steam injection velocity resulted in an increase in pressure drop losses. An increase in steam temperature, on the other hand, led to decreased pressure drop losses. Additionally, an increase in steam dryness fraction resulted in reduced pressure drop losses. Furthermore, it was noted that all pressure drop losses remained below 10%.

https://doi.org/10.1021/acsomega.3c01835
ACS Omega 2023, 8, 44485−44496

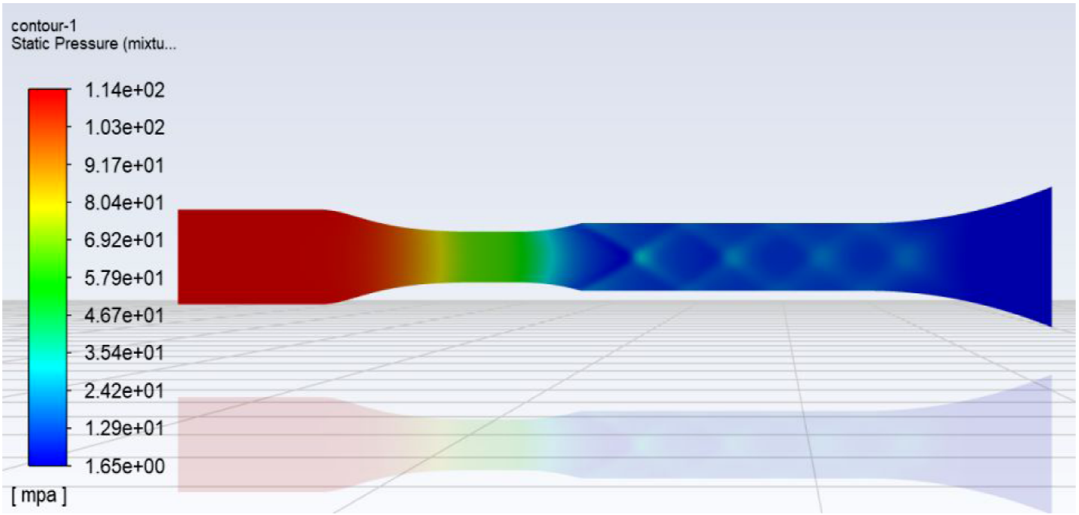

Figure 11. Pressure nephogram with a throat diameter of 3 mm during steam huff-*n*-puff.

During the steam huff-*n*-puff in horizontal wells, numerical simulations were conducted to obtain the velocity and pressure fields inside the supersonic steam injection nozzle with a throat diameter of 3 mm, as shown in Figures 10 and 11. The simulations were performed with a steam injection velocity of 5 t/h, steam injection temperature of 200 °C, and steam injection dryness of 0.5. According to the simulation results, the steam entered the nozzle at subsonic velocity and then accelerated in the tapering section until it reached sonic velocity at the throat, and this process decreased the pressure. Upon entering the diverging section, the steam further accelerated to supersonic velocity, accompanied by the generation of shockwaves, leading to a further decrease in pressure.

6. CONCLUSIONS

(1) The supersonic injection steam nozzle structure consisted of a tapering section, throat, and diverging section. In this study, a mathematical model was developed to calculate the dimensions of the nozzle, allowing for the calculation of lengths and dimensional parameters for each section. Through numerical simulations, the optimal geometry for the tapering section was determined to be a Witoszynski curve. Based on engineering experience, the throat was designed as a straight parallel section, while the diverging section was designed as a straight line with a gradually expanding angle.

(2) By combining the aerodynamic equations with optimized dimensional parameters, the velocity-Mach number and saturation temperature-saturation pressure were calculated for different throat diameters. The results indicated that when steam flowed through the supersonic injection steam nozzle, both the velocity and Mach number increased, with a sharp increase in velocity at the throat. The saturation temperature and saturation pressure decreased gradually, and the temperature and pressure decreased more rapidly in the converging section with larger throat diameters.

(3) Based on the well-clustered relationship between steam Reynolds number and axial−radial dimensions, three nozzle sequences were obtained: 3, 5, and 6.5 mm. Among them, for a throat diameter of 5 mm, the tapering section length was determined to be 4.3 mm, the diverging section length was 5.5 mm, the throat length was 3 mm, the inlet diameter was 9.8 mm, and the outlet diameter was 6.2 mm. Through numerical simulations, the pressure drop was calculated for different steam injection conditions, and the results showed that the pressure drop was within 10%, validating the rationality of the optimized design of the nozzle structure.

AUTHOR INFORMATION

Corresponding Author

Zhanxi Pang − *State Key Laboratory of Petroleum Resources and Engineering, China University of Petroleum, Beijing 102249, China;* orcid.org/0000-0002-1438-360X; Email: pxiad9827@163.com

Authors

Qianhui Wang − *State Key Laboratory of Petroleum Resources and Engineering, China University of Petroleum, Beijing 102249, China*

Cong Tian − *Tianjin Branch of China National Offshore Oil Company (CNOOC) Ltd., Tianjin 300452, China*

Jiajie Chen − *State Key Laboratory of Petroleum Resources and Engineering, China University of Petroleum, Beijing 102249, China*

Complete contact information is available at: https://pubs.acs.org/10.1021/acsomega.3c01835

Notes

The authors declare no competing financial interest.

ACKNOWLEDGMENTS

The study was supported by the National Natural Science Foundation of China (52074321) and the Natural Science Foundation of Beijing Municipality, China (3192026).

REFERENCES

(1) Bai, Y.; Cao, G.; An, H.; Zhang, H. Generation laws and distribution characteristics of carbon dioxide hydrate in a reaction kettle. *Exp. Therm. Fluid Sci.* **2020**, *116*, 110125.

(2) Liu, H.; Dong, X. Current status and future trends of hybrid thermal EOR processes in heavy oil reservoirs. *Pet. Sci. Bull.* **2022**, *7*, 174−184.

https://doi.org/10.1021/acsomega.3c01835
ACS Omega 2023, 8, 44485−44496

(3) Liu, Z.; Wang, H.; Blackbourn, G.; Ma, F.; He, Z.; Wen, Z.; Wang, Z.; Yang, Z.; Luan, T.; Wu, Z. Heavy oil and oil sands: global distribution and resource assessment. *Acta Geol. Sin. (Engl. Ed.)* **2019**, *93* (1), 14.
(4) Wang, X.; Zhang, G.; Tang, W.; Wang, D.; Wang, K.; Liu, J.; Du, D. A review of commercial development of continental shale oil in China. *Energy Geosci.* **2022**, *3* (3), 282−289.
(5) Zhao, F.; Liu, Y.; Lu, N.; Xu, T.; Zhu, G.; Wang, K. A review on upgrading and viscosity reduction of heavy oil and bitumen by underground catalytic cracking. *Energy Rep.* **2021**, *7*, 4249−4272.
(6) Zhang, N.; Liu, W.; Zou, X.; Wang, S.; Sun, Q.; Li, B.; Li, S.; Bhusal, A.; Wang, S.; Li, Z. Experimental study on thermochemical composite system huff-n-puff process in ultra-heavy oil production. *Fuel* **2023**, *332*, 126014.
(7) Zhang, B.; Xu, C.-M.; Liu, Z.-Y.; Zhao, Q.-H.; Cheng, H.-Q.; Li, Y.-Q.; Shi, Q. Mechanism investigation of steam flooding heavy oil by comprehensive molecular characterization. *Pet. Sci.* **2023**, *20*, 2554−2563.
(8) Shi, L.; Ma, D.; Liu, P.; Li, X.; Xi, C.; Wang, C. Experimental and numerical simulation studies on effects of viscosity reducers for steam assisted gravity drainage performances in extra-heavy oil reservoirs. *J. Pet. Sci. Eng.* **2019**, *173*, 146−157.
(9) Nie, B. A comprehensive model for simulating supercritical water flow in a vertical heavy oil well with parallel double tubes. *J. Pet. Sci. Eng.* **2021**, *205*, 108790.
(10) Zhang, L. N.; Du, D. F.; Zhang, Y. Z.; Liu, X.; Fu, J. G.; Li, Y.; Ren, J. H. Steam cavity expansion model for steam flooding in deep heavy oil reservoirs. *Energies* **2022**, *15* (13), 4816.
(11) Osma, L.; García, L.; Pérez, R.; Barbosa, C.; Botett, J.; Sandoval, J.; Manrique, E. Benefit−cost and energy efficiency index to support the screening of hybrid cyclic steam stimulation methods. *Energies* **2019**, *12* (24), 4631.
(12) Wu, S. G.; Dong, D. D.; Yu, Z. H.; Zou, D. B. Geophysical evaluation methods for buried hill reservoirs in the Jiyang super-depression of the Bohai Bay basin, eastern China. *J. Geophys. Eng.* **2007**, *4* (2), 148−159.
(13) Haiyan, H.; Shuhong, W.; Yitang, Z.; Dingmin, W.; Zhong, G. State-of-the-art of heavy-oil development in China and its technology challenges. *International Petroleum Technology Conference*, 2005 10.2523/iptc-10617-ms.
(14) Li, M.; Zhou, F.; Dong, E.; Zhang, G.; Zhuang, X.; Wang, B. Experimental study on the multiple fracture simultaneous propagation during extremely limited-entry fracturing. *J. Pet. Sci. Eng.* **2022**, *218*, 110906.
(15) Huang, S. J.; Cao, M.; Cheng, L. S. Experimental study on the mechanism of enhanced oil recovery by multi-thermal fluid in offshore heavy oil. *Int. J. Heat Mass Transfer* **2018**, *122*, 1074−1084.
(16) Ren, L.; Jiang, H.; Zhao, J.; Lin, R.; Wang, Z.; Xu, Y. Theoretical study on fracture initiation in deep perforated wells with considering wellbore deformation. *J. Pet. Sci. Eng.* **2022**, *211*, 110141.
(17) Shi, X.; Song, W. Q.; Xu, H. X.; Guo, T. K.; Feng, Q. H.; Wang, S.; Jiang, S. The impact of variable density in-plane perforations on fracture propagation and complexity control in the horizontal well. *J. Pet. Sci. Eng.* **2022**, *212*, 110211.
(18) Li, M.; Zhou, F. Multi-fracture initiation sequence and breakdown pressure in horizontal wells during TDPF: a visualization experimental investigation based on PMMA. *J. Pet. Sci. Eng.* **2022**, *215*, 110645.
(19) Xi, X.; Yang, S. T.; Shipton, Z.; Cai, M. F. Modelling the near-wellbore rock fracture tortuosity: role of casing-cement-rock well system, perforation and in-situ stress. *Int. J. Rock Mech. Min. Sci.* **2022**, *157*, 105182.
(20) Al Hadabi, I.; Sasaki, K.; Sugai, Y.; Yousefi-Sahzabi, A. Steam trap control valve for enhancing steam flood performance in an Omani heterogeneous heavy oil field. *J. Unconv. Oil Gas Resour.* **2016**, *16*, 113−121.
(21) Qian, J.-y.; Wei, L.; Zhang, M.; Chen, F.-q.; Chen, L.-l.; Jiang, W.-k.; Jin, Z.-j. Flow rate analysis of compressible superheated steam through pressure reducing valves. *Energy* **2017**, *135*, 650−658.
(22) Zhang, Y.; Li, P.; Sun, X.; Chen, H.; Liu, Y. Steam conformance investigation of flow control devices deployed in SAGD injection and production horizontal wells. *J. Pet. Sci. Eng.* **2021**, *205*, 108907.
(23) Liu, D. Uniform steam injection technology for heavy oil horizontal wells. *Spec. Oil Gas Reservoirs* **2014**, *21*(5).
(24) Wu, Y.; Li, X.; Sun, X.; Ma, D.; Wang, H. Key parameters forecast model of injector wellbores during the dual-well sagd process. *Pet. Explor. Dev.* **2012**, *39* (4), 514−521.
(25) Hight, M. A.; Redus, C. L.; Lehrmann, K. Evaluation of dual-injection methods for multiple-zone steamflooding. *SPE Reservoir Eng.* **1992**, *7* (01), 45−51.
(26) Dong, X.; Liu, H.; Chen, Z.; Wu, K.; Lu, N.; Zhang, Q. Enhanced oil recovery techniques for heavy oil and oilsands reservoirs after steam injection. *Appl. Energy* **2019**, *239*, 1190−1211.
(27) Zhang, N.; Li, H.; Dong, W.; Wang, N.; Tan, Y. A novel design for a selective fluid inflow control device. *Geoenergy Sci. Eng.* **2023**, *224*, 211657.
(28) Burke, L.; Ghazar, C. Flow control devices in SAGD-A system-based technology solution. In *Proceedings of the SPE Thermal Well Integrity and Design Symposium*: Banff, Alberta, Canada, 2018; pp 1−12.10.2118/193353-MS.
(29) Qian, J.-y.; Hou, C.-w.; Mu, J.; Gao, Z.-x.; Jin, Z.-j. Valve core shapes analysis on flux through control valves in nuclear power plants. *Nucl. Eng. Technol.* **2020**, *52* (10), 2173−2182.
(30) Qian, J.-y.; Wu, J.-y.; Gao, Z.-x.; Jin, Z.-j. Effects of throttling window on flow rate through feed-water valves. *ISA Trans.* **2020**, *104*, 393−405.
(31) Irani, M.; Sabet, N.; Bashtani, F. Horizontal producers deliverability in SAGD and solvent aided-SAGD processes: pure and partial solvent injection. *Fuel* **2021**, *294*, 120363.
(32) Lastiwka, M.; Bailey, C.; James, B.; Zhu, D. A practical approach to the use and design of flow control devices in SAGD. In *SPE Canada Heavy Oil Technical Conference 2017, February 15, 2017−February 16, 2017*; Society of Petroleum Engineers: Calgary, AB, Canada, 2017; pp 777−789.10.2118/185005-ms.
(33) Temizel, C.; Canbaz, C. H.; Palabiyik, Y.; Irani, M.; Balaji, K.; Ranjith, R. Production optimization through intelligent wells in steam trapping in SAGD operations. In *Proceedings of the SPE Western Regional Meeting, SPE195361*: San Jose, California, USA, 2019; pp 1−36.10.2118/195361-MS.
(34) Stalder, J. L. Test of SAGD flow distribution control liner system, Surmont Field, Alberta, Canada. In *Proceedings of the SPE Western Regional Meeting, SPE153706*: Bakersfield, California, USA, 2012; pp 1−9.10.2118/153706-MS.
(35) Gorham, T.; Sims, J.; Buell, R. S.; Miller, R.; Fermaniuk, B.; Heukelman, H. Horizontal steam injection liner deployed flow control device design development and testing. In *SPE Thermal Well Integrity and Design Symposium*; Society of Petroleum Engineers, 2019, November17.
(36) Yusuf, Y.; Roostaei, M.; Soroush, M.; Rosi, G.; Berner, K.; Tegegne, N.; Mohammadtabar, F.; Izadi, H.; Zhu, D.; Mahmoudi, M.; et al. Single and multi-phase flow loop testing for characterization and optimization of flow control devices used in SAGD: the effect of viscosity and gas-to-liquid ratio on tool performance. In *SPE Thermal Integrity and Design Symposium*, Day 3 Thu, January 28, 2021.
(37) Zhu, D. A dual-directional flow control device for cyclic steam stimulation applications. *SPE Prod. Oper.* **2022**, *37* (01), 151−158.
(38) Gohari, K.; Becerra Moreno, O.; Romanova, U.; O'Hagan, D.; Mende Anjaneyalu, A.; Gaviria, F. Technical review of tubing deployed flow control devices at MacKay River. In *SPE Annual Technical Conference and Exhibition*, 2019.10.2118/196212-ms.
(39) Su, W.; Liu, T. Temperature, internal energy, entropy and laws of thermodynamics. *J. Univ. Electron. Sci. Technol. China* **1997**, *000* (0S1), 257−260.
(40) Sung, B.-K.; Jeong, S.-M.; Choi, J.-Y. Direct-connect supersonic nozzle design considering the effect of combustion. *Aerosp. Sci. Technol.* **2023**, *133*, 108094.
(41) Abdul-Jabbar Alhodali, M. Preliminary design and simulation of an innovative rotary supersonic nozzles expander apparatus for natural

https://doi.org/10.1021/acsomega.3c01835
ACS Omega 2023, 8, 44485−44496

gas liquefaction and general refrigeration processes. *Appl. Therm. Eng.* **2023**, *222*, 119755.
(42) Li, Y. F.; Deng, J. Q. Numerical investigation on the performance of transcritical CO_2 two-phase ejector with a novel non-equilibrium CFD model. *Energy* **2022**, *238*, ARTN 121995.
(43) Foelsch, K. The analytical design of an axially symmetric Laval nozzle for a parallel and uniform jet. *J. Aeronaut. Sci.* **1949**, *16* (3), 161−166 (acccessed 2023/06/29).
(44) Verma, K. A.; Pandey, K. M.; Ray, M.; Sharma, K. K. Numerical investigation on the effect of variation of upper wall divergence angle of parallel fuel injection scramjet combustor performance. *Int. J. Thermofluids* **2022**, *15*, 100179.
(45) Liu, Z.; Favrel, A.; Miyagawa, K. Effect of the conical diffuser angle on the confined swirling flow induced precessing vortex core. *Int. J. Heat Fluid Flow* **2022**, *95*, 108968.
(46) Chen, J.; Jiang, W.; Han, C.; Liu, Y. Numerical study on the influence of supersonic nozzle structure on the swirling condensation characteristics of CO_2. *J. Nat. Gas Sci. Eng.* **2021**, *88*, 103753.
(47) Wang, S.; Xiao, D.; Qiu, S.; Zhang, X.; Li, X.; Hung, D. L. S.; Xu, M. The effects of nozzle taper angle on in-nozzle flow and nozzle tip-wetting under flash boiling conditions. *Fuel* **2022**, *329*, 125348.
(48) Zhang, G.; Dykas, S.; Yang, S.; Zhang, X.; Li, H.; Wang, J. Optimization of the primary nozzle based on a modified condensation model in a steam ejector. *Appl. Therm. Eng.* **2020**, *171*, 115090.
(49) Cao, X.; Liu, Y.; Zang, X.; Guo, D.; Bian, J. Supersonic refrigeration performances of nozzles and phase transition characteristics of wet natural gas considering shock wave effects. *Case Stud. Therm. Eng.* **2021**, *24*, 100833.
(50) Chen, S. H.; Chen, J. P.; Chen, G. L. Experimental determination of the critical steam Reynolds number in helically coiled tubes. *Int. J. Heat Mass Transfer* **1999**, *42*, 1791−1800.

https://doi.org/10.1021/acsomega.3c01835
ACS Omega 2023, 8, 44485−44496